npj | clean water

www.nature.com/npjcleanwater

ARTICLE OPEN

Check for updates

Scalable and high throughput photothermal water disinfection with negligible CO_2 footprint utilizing nanostructured carbon coatings

Ananya Sah[1], Atindra Kanti Mandal[2], Shubham Tiwari[1], Soumyo Mukherji[3]✉ and Chandramouli Subramaniam[1]✉

Water heating and disinfection with reduced energy and CO_2 footprint demands new and efficient materials for solar-thermal conversion technologies. Here, we demonstrate nanostructured porous hard-carbon florets (NCF) as effective solar absorber coating achieving excellent photon thermalization efficiency (87%). Functional NCF coating on three-dimensionally tapered helical solar receivers generate high surface temperatures (up to 95 °C). Such 'green-heat' is channeled to heat water up to 82 °C that simultaneously results in water disinfection through thermal shock. Untreated lake-water with high turbidity (5 NTU), high bacterial load (10^6 CFU mL^{-1}) and pathogenic fungi is effectively disinfected in a continuous flow process. Translating this, a fully automated SWAP prototype (solar water antimicrobial purifier), delivers bacteria free hot water at an output capacity of 42 L m^{-2} day^{-1} with the lowest CO_2 footprint (5 kg L^{-1}) in comparison to all other existing approaches (>40 kg L^{-1}).

npj Clean Water (2023)6:75 ; https://doi.org/10.1038/s41545-023-00284-4

INTRODUCTION

Hydrogen bonding, dipole moment, its ability to support life and its ubiquitous presence contributes to its extensive contamination by a wide variety of chemical, microbes, inorganic and organic materials[1–3]. As the cradle of all life-forms, that sustains the continuous evolution of human civilization, water has borne the brunt of increased anthropogenic activities and has turned into the most-contaminated chemical on earth[2,4]. Universally, this has resulted in severely restricted access to clean and affordable water, with over 25% of the global population lacking clean water for domestic usage[5,6]. Coupled with deteriorating climatic conditions driven by global warming the need for achieving a positive water-energy nexus becomes critical, to achieve equitable and sustainable development. This is further emphasized by the demand of clean water being an essential prerequisite for meeting seven of the 17 verticals under the United Nations-Sustainable Development Goals[7].

Microbial contamination contributes to ~80% of global water scarcity, annually accounting for ~2.8 million deaths (4%) globally[8,9]. Heating constitutes the primary route for disinfecting water, with world health organization (WHO) recommending full rolling boil for at least one minute before consumption[10,11]. The thermal energy for this process is predominantly derived from combustion of non-renewable fuels, leading to its emergence as one of the largest contributors to global CO_2 emissions (46%)[12]. In addition, the secondary effects of the obnoxious gases released during combustion of such non-renewable fuels lead to severe respiratory problems[11–13]. Therefore, realizing heating of water with positive water-energy nexus constitutes an important step towards sustainable development.

In this scenario, solar energy is grossly under-utilized and forms an attractive source to convert and generate non-polluting thermal energy for water purification with a significantly positive water-energy nexus[13,14]. Although, solar-water distillation and associated disinfection is ubiquitous in nature, it suffers from lower heating efficiency (5 L m^{-2} day^{-1}), intrinsically intermittent nature, requirement of large area and possibility of introducing other heavy metal contaminants such as Cr(VI)[15–17]. Furthermore, the design of the solar-water heater have remain unchanged over the past three decades due to limitations in generating coatings of solar absorbers (mainly chromium-based)[18,19]. This design incorporates multi-level architecture consisting of multiple metal coatings to increase absorption and vacuum cladding to reduce radiative losses[19,20]. Thus, scalable and viable use of solar-energy for disinfecting water has been a distant and challenging reality. These design restrictions extend to solar-thermal distillation systems resulting in poor water output ranging from 5–7 L m^{-2} day^{-1} that is far below the average domestic requirement of 20 L m^{-2} day^{-1}[15–17,21].

The recent decade has witnessed the extensive use of short-wavelength, ultra-violet segment of electromagnetic radiation (200–400 nm) for germicidal and viral disinfection of water[22]. The extensive use of plastics along with the ultra-violet radiation has added yet another dimension of emerging contaminants to water such as carcinogenic benzene, bis-phenol A, fluorinated alkanes and neurogenic volatile organic compounds that arises from UV-induced degradation of the plastics[23–25]. In addition to requiring electrical power to operate, the efficiency of action for this line-of sight technique drastically degrades with turbid water (>5 NTU), due to higher attenuation of the ultraviolet rays[22,26]. Furthermore, turbidity is often associated with microbial contamination and also degrades the lifetime of the device through extensive biofouling, surface passivation and corrosion[26]. An alternative scalable strategy lies in chlorination to disinfect water. Although affordable and scalable chlorination is often associated with downstream microbial regrowth due to which excessive chlorination has become the standard recommendation by WHO[22,27]. This creates additional problems due to generation of carcinogenic by-

[1]Department of Chemistry, Indian Institute of Technology Bombay, Powai, Mumbai 400076, India. [2]Department of Centre for Research in Nanotechnology and Science, Indian Institute of Technology Bombay, Powai, Mumbai 400076, India. [3]Department of Bioscience and Bioengineering, Indian Institute of Technology Bombay, Powai, Mumbai 400076, India. This study is dedicated to Professor Thalappil Pradeep on the occasion of his 60th birthday. ✉email: mukherji@iitb.ac.in; csubbu@chem.iitb.ac.in

products such as halogenated trihalomethanes (THMs) and haloacetic acids (HAAs)[27].

Contact-based techniques uses a range of materials such as zeolites[28,29], polymer-based materials[30], metal and metal-oxide nanoparticles (Ag, Zn, Au, Cu and Fe) for their antimicrobial properties[31–40]. In this context, the nanoparticle-based remediation is effective against both Gram-negative and Gram-positive bacteria and proceeds through surface-mediated rupture of the cellular membrane[28–42]. Efforts have been made to target broad spectrum of microbes such as Gram-negative *Proteus refrigere*, *Pseudomonas aeruginosa* and Gram-positive *Staphylococcus aureus* and *Streptococcushaemolyticus* through appropriate combination with carbon nanoparticles and chitosan[37]. It is imperative for the impure water to directly contact with these surfaces to ensure bacterial decontamination, due to surface based bactericidal effect of all these materials leading to biofouling, degradation of activity and necessitating longer processing time. A persistent challenge with all such contact-based techniques is the requirement to regenerate the active antimicrobial surface and simultaneously minimize bio-fouling[43].

Solar water heating and disinfection, addresses all these drawbacks of various techniques. Solar thermal coatings demand material with high absorption ability in the broadband range and effectively converting solar energy to light energy. Most coatings are black nickel, black chromium or a combination of metal and metal oxide coating[44–58]. Such coating absorbs at selective wavelengths and undergoes rapid degradation under humid condition. Protective ethylene-propylene-diene coating to prevent degradation, leads to increased thermal losses, thus decreasing the efficiency[46–58]. Some coating involves multi-layer coating[57]. The ability to harness solar energy to produce green-heat has been severely limited due to non-availability of appropriate materials. This has been major bottleneck that impedes the rate of water remediation, throughput efficiency, antimicrobial efficacy and thereby limits practical large-scale implementation. Focussing on this, we recognized that efficient solar-thermal conversion demand materials that are broadband absorbers with low thermal conductivity and high thermal effusance. Inability to realize materials with such mutually exclusive properties has led to larger emphasis on thermal management solutions involving cumbersome vacuum jacketing that also attenuates the incident light. Recognizing these challenges, our approach to designing near-perfect blackbody absorbers relied on both morphological tailoring for greater light entrapment and structural engineering for higher η_{STC}.

Overcoming these drawbacks, solution processable coatings of nanostructured, porous hard-carbon florets (NCF) that exhibit strong broadband absorption (~95%) of sunlight (250–2500 nm) and excellent η_{STC} (87%) is reported here. Thin (5 µm) and conformally uniform, spray-painted NCF coating over hollow aluminum tubes (NCF-Al) bent in a tapered helical geometry generates surface temperatures up to 95 °C under solar illumination. Water flowing through this assembly is thus solar-heated up to 75 ± 7 °C resulting in a significantly lower CO_2 footprint (5 kg L^{-1}) compared to conventional natural gas-based heating (>40 kg L^{-1}). Importantly, the water temperature achieved also leads to 99.99% bacterial (*Escherichia coli*, *e coli*) disinfection of the water. Both water heating and disinfection are achieved in a continuous flow process with a throughput of 73 L m^{-2} day^{-1}. The process avoids biofouling, is effective against water with both high bacterial load (10^6 CFU mL^{-1}) and turbidity (5 NTU) without causing any additional contamination. A portable battery-operated prototype termed as solar water antimicrobial purifier (SWAP) consisting of the functional unit interfaced with indigenously developed flow controller and thermocouple constantly monitors the outlet temperature and ensures rapid heating and broadband disinfection of water from fungal, bacterial and microbial pathogens (Supplementary Table 1). The effectiveness of SWAP using real time water drawn from Powai lake to achieve an overall positive water-energy nexus at a cost of 0.002 USD L^{-1} and expected lifetime of 8 years (calculation in supplementary file) is demonstrated.

RESULTS AND DISCUSSION

Fabrication and characterization of NCF

All these design principles are successfully integrated into a single material via a single step carbon deposition onto sacrificial amorphous dendritic fibrous nanosilica (DFNS) as template through chemical vapor deposition (CVD)[59–65]. The usage of carbon source (acetylene) with high diffusion coefficient (0.9 cm^2 s^{-1}) at high temperature (740 °C) ensures complete percolation of gas-phase precursors of carbon into the dendritic, porous silica network in a rapid, conformal and uniform fashion (Fig. 1a). Subsequent complete removal of DFNS (High-angle annular dark-field imaging, HAADF, Fig. 1b) through NaOH etching liberates chemically stable, porous (867.5 m^2 g^{-1}, Supplementary Fig. 1), monodispersed nanostructures (Fig. 1c) that exhibit complementary, open framework with interconnected folded lamellae arranged in the form of a marigold, that are henceforth referred to as nanostructured carbon florets (NCF, Fig. 1d). Each folded lamella of NCF radiates outward from the center thereby providing a conical assembly with graded porosity that closely mimics the structural aspects of optical microcavity. TEM images depict domains of graphitic short-range ordering (~0.4 nm, Figs. 1e, f, Supplementary Fig. 2) which are randomly oriented at long-range to result in a hard-carbon network that is non-graphitizable under electron-beam irradiation (300 keV, 170 µA, Supplementary Fig. 2). The chemical homogeneity and complete removal of SiO_2 was also confirmed through both the high-angle annular dark-field imaging (HAADF) of isolated NCF and X-ray photoelectron spectroscopy of its ensemble exhibiting the C1s peak at 284.0 eV corresponding to sp^2 C=C framework (Fig. 1g). This is also supported from the absence of any peak corresponding to SiO_2 in the XPS (Supplementary Fig. 3). Thermogravimetric analysis of NCF in air was also carried out. Given then thermal stability of SiO_2, any trace of it would be recorded as remnant weight from such an experiment. Complete combustion of NCF leading to nil-weight beyond 583 °C was observed in the trace, confirming the absence of any bulk-level SiO_2 or other impurities (Supplementary Fig. 4). Similarly, Fourier transform infrared spectroscopy (FT-IR) of NCF also reveals the absence of any fingerprint vibration corresponding to Si-O linkage (Supplementary Fig. 5). The Raman spectra exhibits the characteristic D-band and G-band at 1348 cm^{-1} and 1600 cm^{-1}, respectively (Fig. 1h). The presence of disorder contributing directly to the D-band through double resonance Raman (DRR) is confirmed through spectra obtained by varying the excitation wavelength[62,66,67]. Selective and monotonic shift in the spectral position of the D-band along with invariant spectral position for the G-band confirms the presence of long-range disorder and therefore the hard-carbon structure of NCF[62,66–68]. Further, the D-band, originating from DRR process, does not exhibit any dependence on the polarization of the excitation laser. In contrast, the graphitic domains in case of aligned carbon nanotube yarns, exhibit a strong dependence of the D-band intensity on the polarization of the incident excitation laser (Supplementary Fig. 6). The most characteristic aspect of hard-carbons is their non-graphitizability at higher temperatures, in comparison to all other allotropic variations (carbon nanotubes, graphene, fullerenes and diamonds) that undergo thermal conversion to the thermodynamically stable graphitic structure. Accordingly, the Raman spectra (Supplementary Fig. 7) and powder X-ray diffractogram (Fig. 1i) of pristine NCF resembles that of NCF heated to 1200 °C for 3 h, without any evidence of graphitization. This reaffirms the thermally stable, hard-carbon

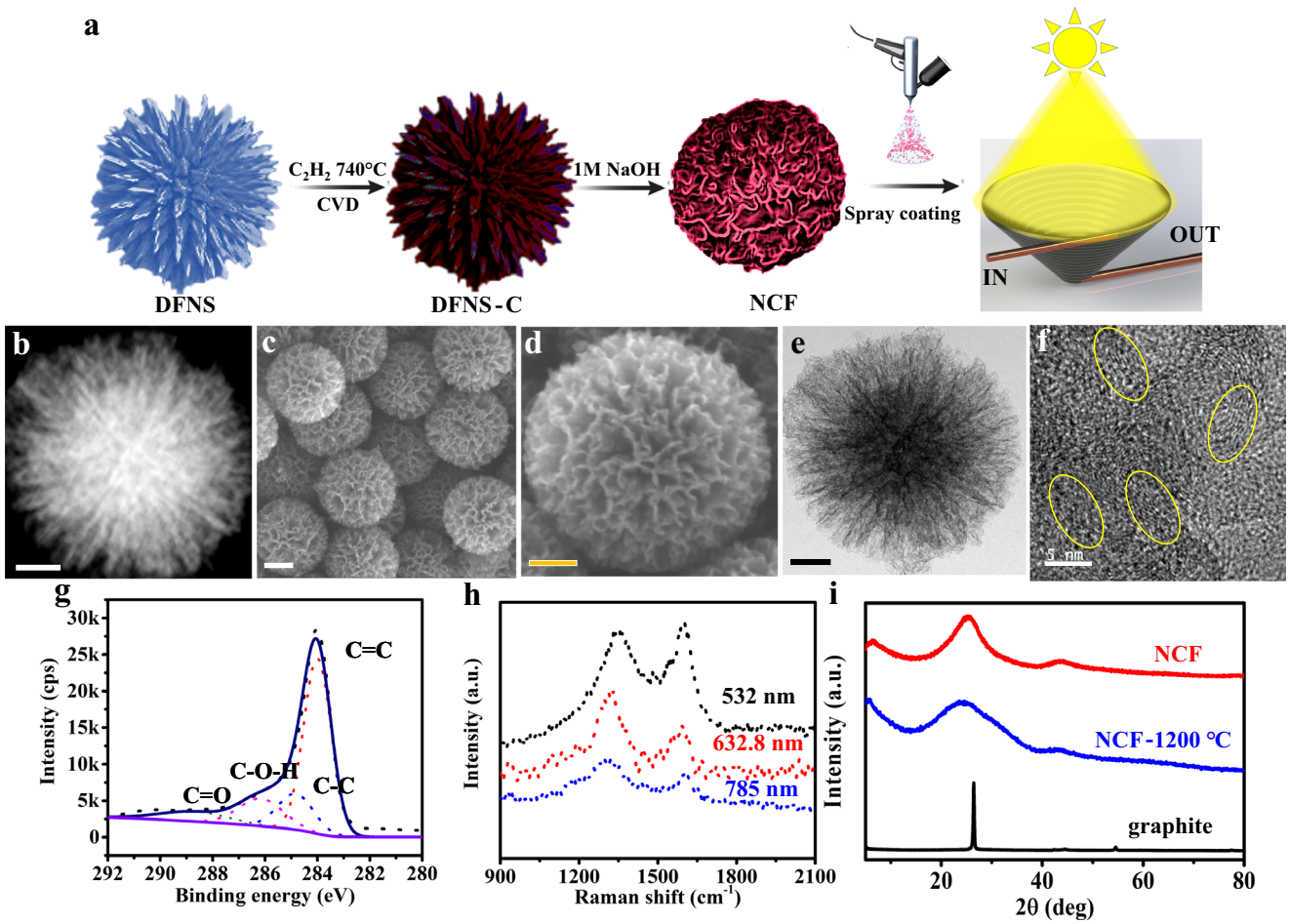

Fig. 1 Synthesis and characterization of NCF. a Schematic for fabrication of NCF, starting from DFNS, going through thermal CVD that is followed by etching of SiO_2 (DFNS). Spray coating of NCF over the tapered helical coil. **b** High-angle annular dark-field imaging, HAADF. Scale bar 100 nm. **c** Sem image of monodisperse NCF. Scale bar 200 nm. **d** SEM images of NCF. Scale bar 100 nm. **e** TEM image of NCF. Scale bar 100 nm. **f** HRTEM images of NCF with the regions of short-range ordering being indicated with yellow rings. Scale bar 5 nm. **g** XPS of NCF. **h** Raman of NCF at different laser excitation. **i** pXRD of the NCF and NCF heated at 1200 °C in comparison to graphite.

structure of NCF. Corroborating these findings in pXRD, the (002) reflection plane (25°) corresponds to expanded graphitic d-spacing of 0.36 nm (Fig. 1i). Furthermore, the large full-width-at-half maximum (8°) of NCF in comparison to graphite (3°, Fig. 1i) indicating a distribution of d-spacing ranging from 0.42 to 0.32 nm in NCF. Further, direct processing of NCF and its application on arbitrary surfaces through spray-coating is achieved without any structural distortions (Supplementary Fig. 8). The coating adhesion to the aluminum substrate was estimated from pull-off adhesion testing to be 5.13 MPa.

The unique morphology consisting of three dimensional conical self-assembly in NCF enhances its absorption over the entire range of solar-spectrum (250–2500 nm). The conical microcavities funnel the incoming photons for greater internal reflection as evidenced by its low transmittance (0.01–4.7%), high absorbance with minimal reflection and diffusance (1.2–6%) over the complete spectral range (Supplementary Fig. 9). Thus, NCF coating functions as near-perfect blackbody absorber to internalize the incident photon energy for subsequent thermalization. Accordingly, a uniform and conformal coating of NCF with thickness of 7 ± 2 µm (surface coverage of 0.8 mg cm^{-2}, Supplementary Fig. 10) was achieved on helically tapered Al tubes (half cone angle 30°, 14 turns). The choice of Al for the flow channel was governed by its high thermal conductivity (205 W m^{-1} K^{-1})[69] and mass density (Fig. 2a). Although Cu exhibits higher thermal conductivity (385 W m^{-1} K^{-1})[69], its intrinsic anti-bacterial property discouraged us from utilizing it, to avoid any potential interference in the observations. The non-illuminated surface of the tapered coil is sheathed with thermally insulating silicone sealant to prevent parasitic convective and radiative heat losses. All the experiments were performed with identical setups under direct solar illumination of 2000 W m^{-2}, unless otherwise specified. The design of the setup maximizes the solar irradiance for a given footprint, while the hollow Al tubes enable the controlled flow of water through the device.

Role of NCF coating on metal substrate for water heating

Upon irradiation, the surface temperature of the NCF-Al is observed to rapidly increase to maximum of 97 ± 7 °C between 8^{th} to 14^{th} turns (Fig. 2b). The surface temperature of the outer turns (1^{st} to 8^{th} turns) is lower (63–90 °C) due to greater radiative loss from the exposed edges (Fig. 2b). Such photon thermalization by NCF occurs with excellent η_{STC} of 87 % and is attributed to the synergistic combination of the conically graded morphology and the hard- carbon structure. Such localized heating is then rapidly transferred through the walls of the Al tube (wall thickness = 1.1 mm) to the water circulating within it. Consequently, the temperature of the water increases linearly with number of turns, generating a maximum surface temperature difference (ΔT^{sur}_{max}) of 52 °C on the 14^{th} turn at a flow rate of 2 mL min^{-1} (Fig. 2c, Supplementary Fig. 11). As expected, the

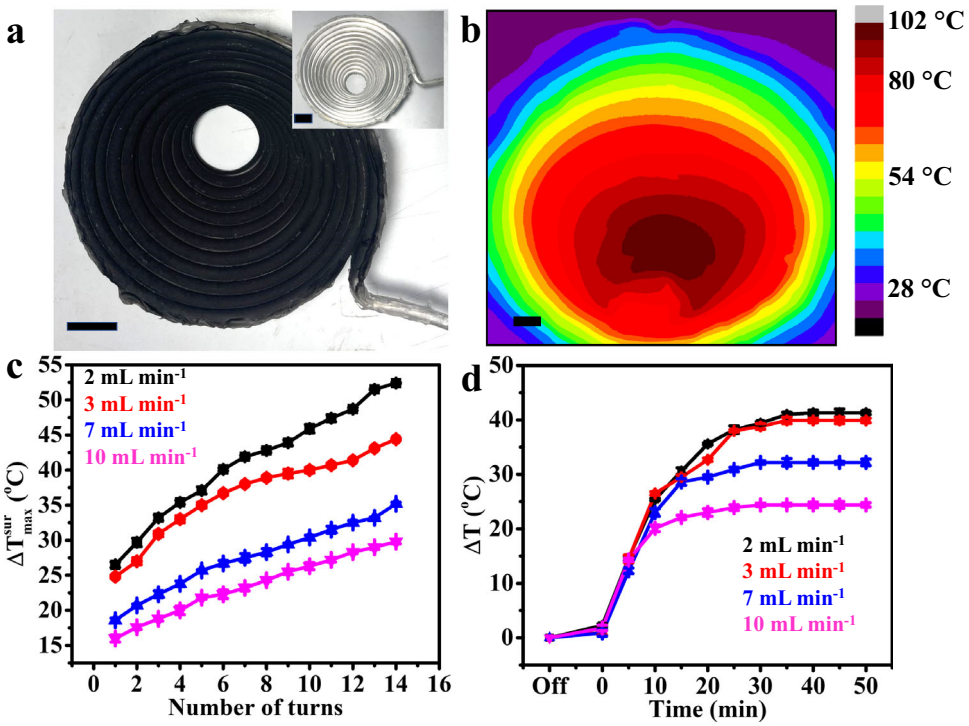

Fig. 2 Photothermal performance of NCF coating. a Photograph of NCF-Al setup. Scale bar 2 cm (Inset: Photograph of uncoated coil, scale bar 2 cm). **b** Surface temperature of NCF-Al coating measured without any water flow through the Al tubes. Scale bar 1 cm. **c** Surface temperature differential measured at various positions of NCF-Al device. **d** Temperature differential of water at the outlet of NCF-Al device. The ambient temperature is 23 °C for **c** and **d**. Error bar are the standard error of the mean.

temperature difference achieved at the outlet is dependent on the flow rate and the number of turns, that determines the residential contact time of water (τ) with the walls of the aluminum tube. Thus, ΔT^{sur}_{max} exhibits a monotonic inverse dependence on the flow rate, with lower ΔT^{sur}_{max} achieved at higher flow rates. The reduced residence time (4 min) at higher flow rates decreases the efficiency of heat transfer to the water and therefore leads to lower ΔT^{sur}_{max}. Nevertheless, the ΔT^{sur}_{max} of 30 °C achieved at a flow rate of 10 mL min^{-1} is still significant for a non-contact-based water heating approach with near-zero CO_2 footprint. Encouraged by these findings, the temperature of the water at the outlet of device was monitored in a continuous flow mode. Consistent with the earlier observations, the water temperature exhibited an initial increase, followed by saturation after 20 min. The maximum outlet temperature difference (ΔT^{out}_{max}) obtained was a function of the flow rate, and saturated at 40 °C for 2 mL min^{-1} (Fig. 2d). Thereafter, the ΔT^{out}_{max} remained constant indicating that the device is effectively able to deliver water continuously at an outlet temperature of 70 °C after an initial lag phase of 20 min. Exhaustive control experiments were carried out both in the absence of light and in the absence of NCF coating, leading to significantly lower ΔT^{out}_{max} (0 °C) and ΔT^{sur}_{max} (0 °C) and thereby establishing the critical ability of NCF in solar-thermal conversion.

Further, additional experiments have been carried out to establish a correlation between the number of turns, flow rates and ΔT^{out}_{max} (Supplementary Fig. 12). Experiments were conducted by varying the number of turns of the Al helical coil and flow rates that directly have bearing on the residence time of the water. Accordingly, irrespective of the number of turns, the ΔT^{out}_{max} decreases with increasing flow rate due to the lowering of residence time. Further, such decrease in ΔT^{out}_{max} is more evident for flow rate above 4 mL min^{-1} which is again attributed to the overall length of the channel that affects the transfer of heat. At flow rate below 4 mL min^{-1}, the ΔT^{out}_{max} reached saturation irrespective of the number of turns. These experiments thereby pinpoint the dependence of ΔT^{out}_{max} on the total length of the coil and the flow rate.

Water containing 2000 ppm Ca^{2+}, in the form of $CaCl_2$, was passed through the NCF-based solar water heater (flow rate = 7 mL min^{-1}) continuously for over 60 h (Supplementary Fig. 13). The total dissolved salt (TDS) content of the outlet water was continuously monitored, along with its temperature. Both these parameters indicated minimal variations (<5% TDS variation and ±2 °C in temperature) over the entire duration of the study. Further, ICP-AES analysis carried out on the outlet water does not exhibit any presence of aluminum and showed minimal (<5%) variation in the concentration of Ca^{2+} and Cl^-.

Investigation of bactericidal effect using NCF-Al device

Having established the ability of device to heat the water utilizing only solar energy through a non-contact approach in continuous flow-through mode of operation, the bactericidal effect of such heating is investigated. Accordingly, buffered water (pH 7.2) that is spiked with known concentrations of *Escherichia coli* (10^4, 10^6 CFU mL^{-1}) was passed through the Al tubes of device (Fig. 3a). Control experiments in the absence of light exhibits no change in the bacterial concentration even after prolonged experiment time scale (40 min) indicating no contribution of the Al tubes to the bactericidal effects observed (Fig. 3a). Control experiments were also conducted with uncoated Al tubes under identical conditions of solar illumination. The outlet temperature of the water from uncoated Al devices under identical conditions is observed to be ~15–20 °C lower than the temperature achieved with NCF-coated devices. Further, the bacterial concentration was observed to remain invariant over time, indicating the inefficiency of uncoated Al tubes towards bacterial decontamination (Fig. 3a). Similarly, direct exposure of sunlight to the bacteria contaminated water (10^4 CFU mL^{-1}) results in near-complete elimination of bacteria

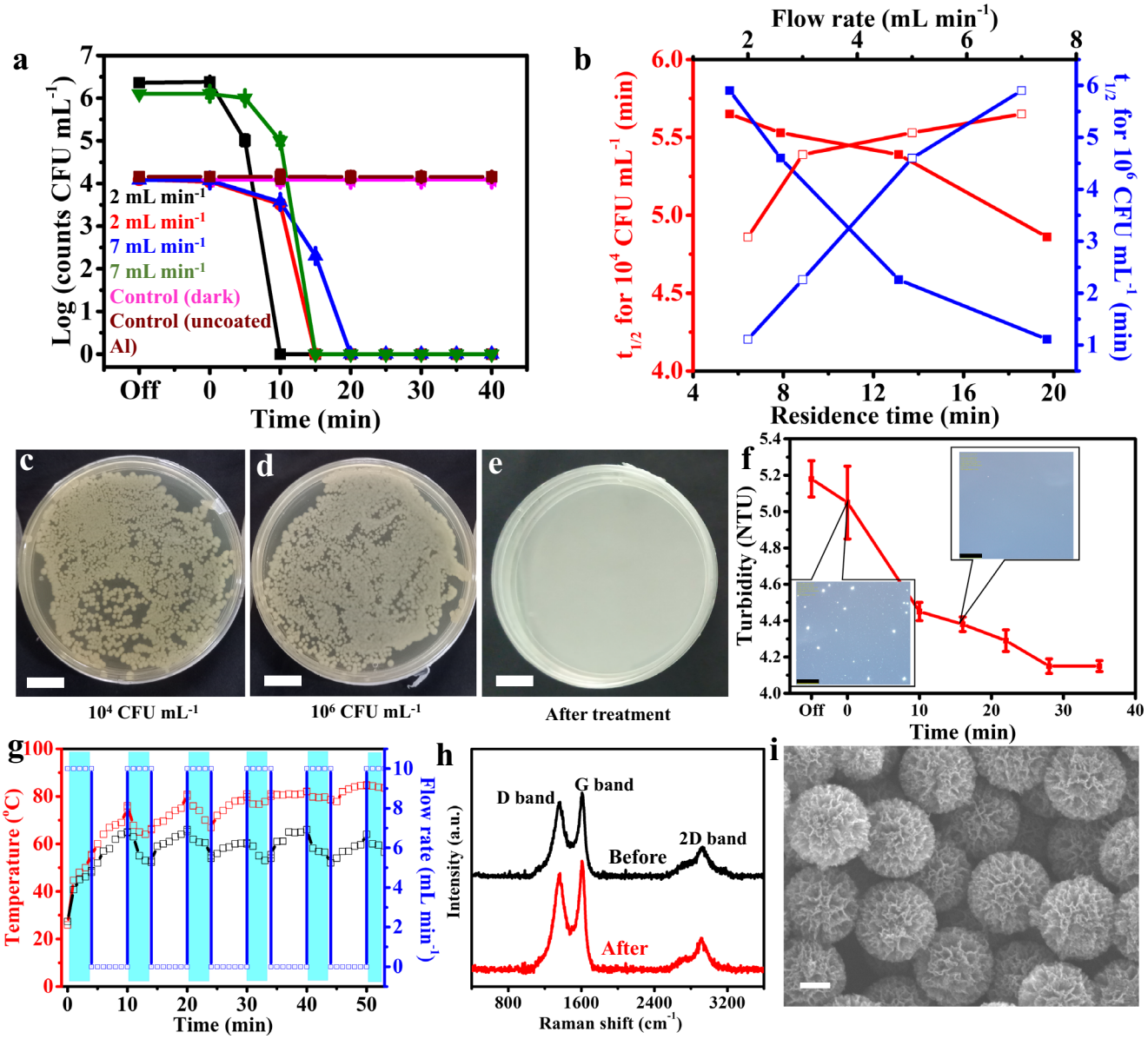

Fig. 3 Water heating based bacterial disinfection with NCF coating. a Change in bacterial concentration with respect to time for the water flowing through the NCF-Al device at various flow rates. The control experiment carried out for uncoated Al device under solar illumination and in dark shows no change in the bacterial concentration for the same time period of experimentation. **b** Variation in $t_{1/2}$ for 10^4 CFU mL^{-1} and 10^6 CFU mL^{-1} with respect to flow rate (hollow) and residence time (solid). Photograph of agar bacterial cell culture plates for **c** 10^4 CFU mL^{-1}, **d** 10^6 CFU mL^{-1} and **e** after flowing through the NCF-Al device. Scale bar 15 mm. **f** Variation in turbidity of water before (OFF) and after flowing through the NCF-Al device (Inset: optical microscopic images of treated water, scale bar 50 µm). **g** Variation of temperature during intermittent flow scheme at the 1st turn (black square) and 14th turn (red square). **h**, **i** Represents the Raman and SEM of NCF coating after the experiment (scale bar 200 nm). Error bar are the standard error of the mean.

after prolonged and continuous exposure of 80 min (Supplementary Fig. 14). In complete contrast to both these control experiments, the bacterial concentration monitored at the outlet of device exhibits a remarkable decrease within 10–15 min of flow under solar illumination, falling below detection limits thereafter (>15 min). This timescale corresponds well with that taken to reach ΔT^{out}_{max} (15 min) is directly correlated to the heating effect produced by NCF. It is to be noted that the induction time required for complete elimination of bacteria exhibits a minor increase at larger flow rate (20 min for 7 mL min^{-1}) compared to smaller flow rate (15 min for 2 mL min^{-1}). Nevertheless, the bactericidal effect would continue to act in the device for any time scale beyond the initial induction time (10–20 min).

Importantly, the device is effective for a wide range of bacterial concentrations that differs by two orders of magnitude. While 10^4 CFU mL^{-1} corresponds to the typically observed concentrations of bacteria in untreated water in Indian conditions, 10^6 CFU mL^{-1} represents the extreme contamination of water and is comparable with that of sewage water[70–72]. Our experiments with 10^6 CFU mL^{-1} surprisingly indicate a smaller induction time (10 min) for complete destruction of bacteria when compared to 10^4 CFU mL^{-1} at the same flow rate. This counter intuitive observations indicates a combined effect of residence time and collision frequency contributing towards the observed bactericidal effects. At lower flow rates (<4 mL min^{-1}), the $t_{1/2}$ reduces significantly with increase in bacterial concentration. This is due to the increase

Table 1. Collision frequency estimated for different flow rates at different bacterial concentration.

Flow rate (mL min^{-1})	Residence Time (min)	Z^a (CFU min^{-1})	Z^b (CFU min^{-1})
2	20.74	2.8×10^4	2.8×10^6
3	13.83	4.2×10^4	–
7	5.93	9.9×10^4	9.9×10^6

[a]Estimated at 10^4 CFU mL^{-1}.
[b]Estimated at 10^6 CFU mL^{-1}.

in collision frequency dictating the heating of the solution leading to faster bactericidal action. In agreement with these observations, the difference in $t_{1/2}$ between 10^6 and 10^4 CFU mL^{-1} reduces at higher flow rates (>4 mLmin^{-1}, Fig. 3b). While residence time pertains to the flux of the water through the Al tubes, the collision frequency refers to the average number of collisions that each bacterial cell undergoes with the walls of the Al channel.

The heat transfer pathway acting in device considers the NCF coating as the heat source and the water as the heat sink, with the Al channel acting as the heat transfer medium. It is evident that the lower induction time observed at higher bacterial concentration (10^6 CFU mL^{-1}) is predominantly contributed from the direct contact of the bacteria with the walls of the channel, as seen from the collision frequency under these conditions (Table 1). Collision Frequency[73],

$$Z = \frac{\pi d^2 \times <c> \times N}{\sqrt{2} \times V} \quad (1)$$

Where, <*c*> is the average speed of molecules, *N* is the number of colonies forming unit, *V* is the volume, *d* is the inner diameter of the coil.

On the other hand, the bactericidal effect observed at lower bacterial concentration (10^4 CFU mL^{-1}) originates mainly due to bulk heating of water, since the estimated collision frequency is lower. These results conclusively establish the bactericidal action of device over a wide range of concentrations. Furthermore, the temperature achieved crosses 80 °C, enabling the complete decontamination of water from a wide range of water-borne microbes that are thermally unstable beyond this temperature (Fig. 3c–e). Importantly, NCF-Al device achieve this entire function with a short induction time, near zero carbon footprint and in a non-contact manner that avoids bio-fouling.

The absence of bacteria after processing through device is clearly seen from the agar culture plates that show negligible colonies after the experiment in contrast to wide spread growth observed in the feedstock solution (Fig. 3c–e). It is also noted that the water processed through device does not show any bacterial growth after storage for more than 14 days, indicating permanent thermal destruction of the bacterial cells in contrast to their temporary deactivation (Fig. 3e).

Significantly, this thermal-based bactericidal effect also overcomes the line-of-sight problems while dealing with optical-based decontamination approaches of turbid solutions. The entire bactericidal action is achieved by thermal energy in this device. This advantage is demonstrated by processing untreated turbid water feedstock containing lactobacillus (4×10^5 CFU mL^{-1}, 5.2 NTU, Fig. 3f) through device. Although there is no change in the turbidity between the inlet (5.2 NTU) and the outlet (4.3 NTU), the clear absence of lactobacillus at the outlet is evident from the optical microscopic images (Fig. 3f). The absence of change in turbidity is due to the active scattering of the dead bacterial content in a manner that is similar to live lactobacillus.

In comparison to contact-based anti-microbial coatings[28–42], NCF-based coating operates by solar-thermal conversion, wherein the bactericidal effect is due to thermal shock. As demonstrated in our studies, the temperature generated on the NCF-coated surface is transferred to the water, through the aluminum walls. This leads to bacterial decontamination. Thus, the impure water is never in direct contact with the active NCF-surface.

In an effort to lower the induction time by minimizing the effect of flow rate and residence time, the geometry of operation of device was changed from continuous-flow mode to intermittent-flow mode. Herein, the flow rate is alternated between ON state (10 mL min^{-1}) and OFF state (0 mL min^{-1}) within a cycle time period of 10 min. We note that the flow rate employed (10 mL min^{-1}) is insufficient for any bactericidal action when employed in continuous flow mode due to the low residence time (4 min) and consequently the sub-threshold outlet temperature (50 ± 3 °C) reached. However, intermittent flow mode employing the same flow rate is effective in raising the outlet temperature to 80 ± 5 °C after 10 min of induction time. Further continuation of such intermittent flow beyond the induction time of 30 min is found to not affect the outlet temperature (82 ± 5 °C, Fig. 3g). Thereby, the intermittent flow mode enables the bactericidal action at higher flow rates. We note that the throughput is higher in continuous flow mode (73 L m^{-2} day^{-1} for 7 mL min^{-1}) when compared to the intermittent flow at 10 mL min^{-1} (42 L m^{-2} day^{-1}). However intermittent flow facilitates accessing of much higher flow rates and is thus expected to match the output of continuous flow mode at a flow rate of 4 mL min^{-1}.

Finally, the structural and morphological stability of NCF after prolonged exposure to solar irradiance and experimentation (40 h of exposure) are ascertained from the Raman spectra (Fig. 3h) and the SEM images (Fig. 3i) that shows invariant characteristics. There was no change in the pH of the water after experimentation indicating no pitting or corrosion of Al from the device. Furthermore, ICP-AES of the water does not exhibit any Al or heavy metal contamination of the water thereby presenting a distinct advantage over commercial solar heating systems (Supplementary Table 2). The ICP-AES of the outlet water is performed for two main reasons. Firstly, it demonstrates that there is no metal-based contamination of the water during its passage through the NCF-coated device. Secondly, the pH and TDS of the water is invariant signifying the robustness and durability of the NCF-coated device (Supplementary Table 2). The high η_{STC} of NCF implies, that the device does not require any vacuum cladding and is therefore, easy to maintain. The bill-of-materials cost for scaling up of device to a community level plant capable of providing 400 L day^{-1} is estimated to be 304 USD (excluding solar panel) and requires an area of 9.2 m^2. While salinity has not been addressed in device, the low cost and simple operation facilitates direct interfacing with similar low power desalination system such as capacitive deionization and sand filters[74,75].

From laboratory scale to market

This concept of a flow-through heating-based disinfection was translated from a proof-of-concept to a fully functional prototype. At its core, Solar Water Antimicrobial Purifier (SWAP) consists of the NCF-coated Al tapered coil connected to a Kamoer Peristaltic Pump (12 V, 250 mA, flow rate of 55 mL min^{-1}) and controlled by an indigenously developed flow controller unit (FCU). The FCU consists of Atmel Atmega 328 P 8-bit AVR microcontroller which is programmed through an Arduino IDE. It is based on C/C++ (code provided in supplementary information). that receives input from the thermocouple placed at the exit of the NCF-coated Al tapered coil (Fig. 4a, b). The flow of water through the SWAP is accordingly regulated with a motor driver (L293D Quadruple Half-H Driver). This feedback ensures that the flow rate of water through the SWAP is appropriately controlled so as to deliver a constant output water temperature of 85 °C (Supplementary Movie 1). The entire unit along with a sand filter is housed within a 3D printed

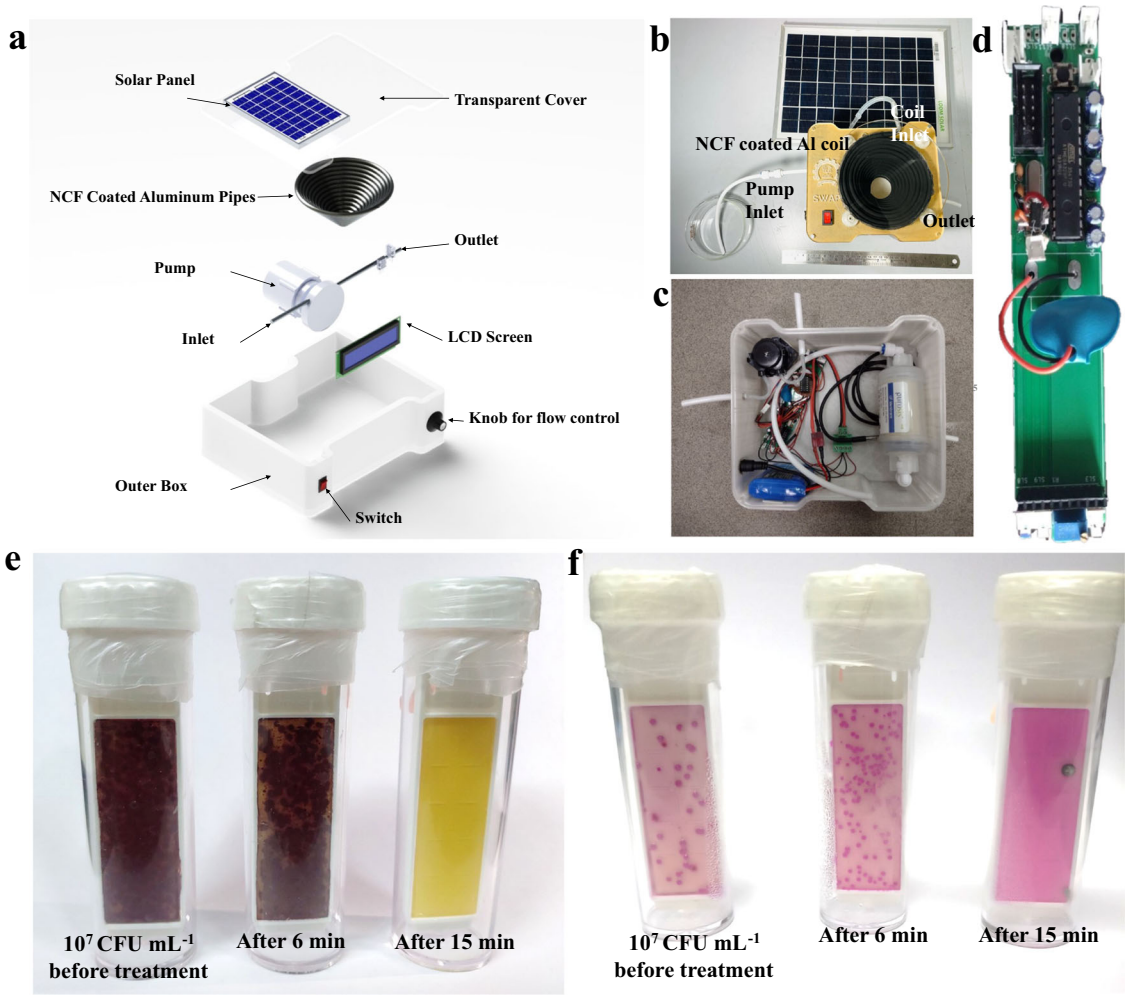

Fig. 4 Assembly and working of SWAP module. a Schematic of SWAP. Photograph of **b** SWAP **c** battery, flow controller unit comprising peristaltic pump, and microcontroller-based PCB and sand filter **d** indigenously developed flow controller. Photograph of bactaslyde kit dipped in Powai-lake water sample representing stock sample (dot indicates microbes), solution collected after 6 min and solution collected after 15 min which is free of microbes (left to right) **e** growth of bacteria over yellow side **f** growth of yeast or fungus over pink side.

chamber resulting in dimensions of length 21 cm, breadth 16 cm, height 10 cm and weight of 452 g. A glass dust-cover was used to minimize maintenance, reduce convective loss and thereby maximize the η_{STC}. This portable unit can be either operated through a 3 Cell Lithium-ion rechargeable battery (11.1 V, 2000 mA h) or powered through solar panel making it entirely self-sustaining (Fig. 4c, d).

Operation of SWAP was conducted in ambient, laboratory conditions (Relative humidity 56%, room temperature 28 °C). Water sample from Powai lake was filtered through a Whatmann filter paper (Grade 1) to remove suspended impurities. The filtrate was passed through SWAP at a flow rate of 2 mL min^{-1} whereby the outlet temperature reaches to 75 ± 7 °C. Since, the water from local pond contains a wide variety of microbes ranging from fungi to bacteria, estimating the bactericidal efficiency of SWAP was carried out using a commercial microbe detection kit (Yeast, fungi and total bacteria count detection, Bactaslyde). While one surface of each slide presents the total bacteria count in the samples, the reverse side gives a qualitative estimate of the yeast and fungal content in the sample. Slides from the test kit were incubated with water samples drawn at different time intervals from SWAP as per the recommended protocol. The photographs of these slides clearly indicate that the near complete reduction in viable microbial content is achieved within 15 min of flow, in agreement with our earlier observations (Fig. 4e, f). These results validate the working of the SWAP prototype and thereby establishes a low-cost, low-power, non-contact based sustainable heating of water leading to its bacterial decontamination.

Pyromark and NALSUN are commercial coating. NCF-based solar-thermal conversion efficiency is 87%, while that of commercially available ETC coatings are 70%[44,45]. This aspect has been used to compare the throughput afforded by both these devices and presented in the Supplementary Tables 3 and 4. The higher efficiency of NCF reflects in terms of higher throughput of hot water compared to existing ETC coatings. This also implies that the land-area required for NCF-based solar-water heaters can be reduced by ~25% for the same throughput of hot-water. Thus, the higher efficiency of NCF-based solar water heaters would either translate to 25% increase in throughput for the same device dimensions or 25% lowering the land-area requirement. Both these aspects are expected to significantly improve the commercial adaptability of solar-water heaters.

In summary, fabrication of NCF was performed via template-based approach which led to short-range ordering and long-range disordering in its intrinsic structure. This enhanced its ability to undergo efficient solar-thermal conversion and effectively deliver the heat to the surface upon which it was coated. The rise in temperature was high enough to undergo water heating along with bactericidal effect without any vacuum lining. This new material and the approach for water heating brings out an

opportunity to replace conventional solar heaters and carry out water disinfection in a much cost-effective manner. The application of it is not limited to water disinfection and can be extended to a newer dimension of studies in context to solar-thermal conversion.

METHODS

Synthesis of nanostructured carbon florets (NCF)

The silica nanospheres were prepared in accordance with the literature[59]. The fabricated nano-silica spheres were kept in a CVD furnace and heated at 740 °C in inert atmosphere. Acetylene (100 SCCM) was flown through as a carbon source. After cooling, the carbon-coated silica nano-spheres obtained was added to NaOH solution (1 M) and stirred to etch out the silica. It was then washed with deionized water. Finally, it was dried to collect the NCF for further characterization.

Preparation of NCF coated tapered helical Al coil (NCF-Al)

A dispersion of NCF in propan-2-ol was prepared using a bath sonicator. A hollow Al coil (length 12 feet, inner diameter 3.8 mm and outer diameter 6 mm) was twisted in the form of tapered helical coil (height 9 cm, upper diameter 130 cm, lower diameter 3 cm) comprising 14 turns with half cone angle of 30°. The tapered helix formed has two regions, the outer region and the inner region. The outer region is covered by silicone sealant to prevent convective heat loss and the inner region is spray-coated with prepared NCF dispersion using spray coater (Fig. 2b) at a temperature of ~90 °C. The coating is uniform as observed from the optical microscopic image (Supplementary Fig. 10). A similar NCF-Al was assembled to form the SWAP prototype as described in the manuscript. The sand filter used in SWAP was procured locally (Purosis uf membrane filter).

Solar-thermal conversion measurements

The NCF-Al was connected to a peristaltic pump and placed under solar irradiation (2000 W m^{-2}) with a glass cover on top (Fig. 1a). Water was flown through the coil at different flow rate 2-, 3-, 7- and 10-mL min^{-1} and the outlet water temperature were recorded using thermocouple. Simultaneous thermometric imaging using FLIR thermal camera was carried out to confirm the measured temperatures.

Estimation of bacterial concentrations

Water (pH 7.2 with phosphate-buffered saline (PBS)) spiked with two concentrations of *Escherichia coli* bacteria (10^4 CFU mL^{-1}, 10^6 CFU mL^{-1}) were used for experiments to estimate the bactericidal efficacy of the device. The concentrations of the bacteria prior to and after the passing through the NCF-Al were estimated through standard agar plate counting method, details of which are provided in supplementary. The control experiment was performed in similar methodology under dark conditions. The experiment with lake water sample was performed using NCF-Al at 2 mL min^{-1} flow rate under 2 sun. The concentration of bacteria was analyzed using microbe detection kit (Bactaslyde).

Building of the prototype

The most important part of the prototype device that was made (called SWAP: Solar Water Antimicrobial Purifier) is the NCF-coated Al pipe through which the water flows, followed by the FCU (flow controller unit), which regulates the flow of water. The rest of the device revolves around these only. FCU consists of a peristaltic pump and a microcontroller-based PCB (printed circuit board) that controls the pump. Since there is a variety of different modes in which the device can be operated, that is it can be a continuous flow method, where water is continuously flowing, or an intermittent flow method, where water is pumped and then held for some time, till the water heats, and then it is discharged, or it can be operated on dynamic mode, where the temperature is actively monitored, and water is only released when it reaches 80 °C. Hence a programmable source to control the pump was needed; therefore, a microcontroller-based flow control unit was designed.

The voltage from the battery or solar panel is first supplied to a voltage regulator (LM1117: low-dropout linear regulator), which generates a stable 5 V required for the microcontroller and other ICs' proper functioning. This 5 V is then supplied to the Atmel Atmega 328 P 8-bit AVR microcontroller. This microcontroller then, based on the operation mode, sends the signals to the motor driver, which drives the pump. The detailed schematic of the circuit is attached in the supplementary document provided (Supplementary Fig. 15). Once the FCU and the coil were made, the rest of the device was designed around it. The mechanical design of the outer box was made to house all the different components properly. A 3D model of the device was made in Solidworks, and then 3D printed. PLA (Polylactic acid) was used as 3D printing material because of its high quality and ease of printing. For the top cover, a 5 mm thick acrylic sheet was used, with a switch to operate the device. After all the different parts were manufactured, everything was assembled and tested.

Characterization

The surface morphology was determined using field emission scanning electron microscopy (FESEM, Zeiss/Ultra 55, 3 keV acceleration voltage). The internal structure characterization and high-angle annular dark-field imaging (HAADF) was performed utilizing Tecnai G2, F30 transmission electron microscope (TEM, 300 keV, acceleration voltage. Witec 300 RAS system was used for acquiring the Raman spectra. The Raman signals were collected using 532 nm laser (Nd-YAG excitation source) in a confocal geometry (300 grooves mm^{-1} grating) on to a Peltier cooled CCD detector, He-Ne diode laser excitation source (632.8 nm) and GaAs-based distributed Bragg reflector 785 nm diode laser. The transmittance, diffuse and total reflectance were determined through Perkin Elmer UV-Vis-NIR Spectrometer - Lambda 950. It consists of integrating sphere mode with PMT (220–860 nm) and InGaAs (860–2500 nm) detector. All thermal images were taken using Forward looking infrared (FLIR A6703sc, Indium Antimonide detector) camera with accuracy of ±2 °C which is calibrated against an electrically heated thermal plate. The camera was placed at a distance of 20 cm throughout the experiment. pXRD characterization was carried out utilizing Rigaku Powder XRD (CuKα radiation, 1.54 Å). The chemical composition of surface was determined through Kratos Analytical Axis Supra X-ray photoelectron spectroscopy (XPS) (monochromatic AlKα X-ray source, 600 W, 1486.6 eV). The thickness of the NCF coating was measured using high defination Olympus microscope of DSX series. The thermogravimetric analysis was carried out using Perkin Elmer (USA) Diamond TG-DTA instrument under air. The adhesion measurement was performed using pull-off adhesion tester. The specific surface area and porosity were measured using Quantachrome Autosorb surface area analyzer. The surface area was determined from N_2 Brunauer−Emmett−Teller (BET) adsorption isotherm at 77 K with analysis time of 24 h. The ICP-AES was carried out using ARCOS, simultaneous ICP spectrometer comprising CCD detector for determination of metal ion concentrations.

DATA AVAILABILITY

All data are available in the main text or the Supplementary Materials.

CODE AVAILABILITY

All codes are available in the Supplementary Material.

Received: 20 April 2023; Accepted: 16 October 2023;
Published online: 03 November 2023

REFERENCES

1. Brini, E. et al. How water's properties are encoded in its molecular structure and energies. *Chem. Rev.* **117**, 12385–12414 (2017).
2. Nathanson, J. A. Water pollution. Encyclopedia Britannica, 18 Oct. https://www.britannica.com/science/water-pollution (2022). Accessed 26 December 2022.
3. Ball, P. *H2O: A biography of water* (Orion Publishing Co; UK, 2000).
4. World Health Organization. Drinking water. https://www.who.int/news-room/fact-sheets/detail/drinking-water (2022).
5. World Health Organization and UNICEF. *Progress on household drinking water, sanitation and hygiene 2000-2020: five years into the SDGs* (World Health Organization (WHO) and the United Nations Children's Fund (UNICEF), 2021).
6. World Health Organization and UNICEF. *Progress on drinking water, sanitation and hygiene in schools* (United States: United Nations Children's Fund (UNICEF) and World Health Organization (WHO) Joint Monitoring Programme for Water Supply and Sanitation, 2020).
7. Jensen, L. United Nations. The sustainable development goals report 2022. Department of Economic and Social Affairs. https://unstats.un.org/sdgs/report/2022/ (2022).
8. Yang, K. et al. Global distribution of outbreaks of water-associated infectious diseases. *PLoS Negl. Trop. Dis.* **6**, e1483 (2012).
9. Murray, K. A. et al. Global biogeography of human infectious diseases. *Proc. Natl Acad. Sci. USA* **112**, 12746–12751 (2015).
10. World Health Organization. Guidelines for drinking-water quality, 4th edition, incorporating the 1st addendum. https://www.who.int/publications/i/item/9789241549950 (2017).
11. García-Gil, Á., García-Muñoz, R. A., McGuigan, K. G. & Marugán, J. Solar water disinfection to produce safe drinking water. A review of parameters, enhancements, and modelling approaches to make SODIS faster and safer. *Molecules* **26**, 3431 (2021).
12. Hannah, R., Max, R. & Pablo, R. CO_2 and greenhouse gas emissions, Our World in Data. https://ourworldindata.org/co2-and-other-greenhouse-gas-emissions (2020).
13. Ferroukhi, R. et al. Renewable energy in the water, energy & food nexus. IRENA. https://www.irena.org/publications/2015/Jan/Renewable-Energy-in-the-Water-Energy--Food-Nexus (2015).
14. Wu, W., Maier, H. R., Dandy, G. C., Arora, M. & Castelletti, A. The changing nature of the water–energy nexus in urban water supply systems: a critical review of changes and responses. *J. Water Clim. Chang.* **11**, 1095–1122 (2020).
15. Solar Water Distillation. *Safe Drinking Water Foundation*. https://www.safewater.org/fact-sheets-1/2016/12/8/solar-water-distillation (2016).
16. Reddy, K. S. & Sharon, H. Energy-environment-economic investigations on evacuated active multiple stage series flow solar distillation unit for potable water production. *Energy Convers. Manag.* **151**, 259–285 (2017).
17. Al-Kharabsheh, S. & Goswami, D. Y. Solar distillation and drying. *Encycl. Energy* **5**, 597–606 (2004).
18. Koyuncu, T. & Lüle, F. Thermal performance of a domestic chromium solar water collector with phase change material. *Procedia Soc. Behav. Sci.* **195**, 2430–2442 (2015).
19. Santamouris, M., Papaioannou, D., Argiriou, A. & Stavrakakis, G. Technical and economical comparison between solar water heaters using electrodeposited chrome selective coating and selective paints. *Energy Convers. Manag.* **30**, 421–431 (1990).
20. Azha, N. I. S., Hussin, H., Nasif, M. S. & Hussain, T. Thermal performance enhancement in flat plate solar collector solar water heater: a review. *Processes* **8**, 756 (2020).
21. Water consumption. *Safe Drinking Water Foundation*. https://www.safewater.org/fact-sheets-1/2017/1/23/water-consumption (2017).
22. Azim, N. et al. Literature review of disinfection techniques for water treatment. In *International Conference on Environmental Systems* (International Conference on Environmental Systems, 2020).
23. Chaisupakitsin, M., Chairat-Utai, P. & Jarusiripot, C. Degradation of polyethylene terephthalate bottles after long sunlight exposure. *Songklanakarin J. Sci. Technol.* **41**, 259–264 (2019).
24. Webb, H. K., Arnott, J., Crawford, R. J. & Ivanova, E. P. Plastic degradation and its environmental implications with special reference to poly(ethylene terephthalate). *Polymers* **5**, 1–18 (2013).
25. Mondal, S. & Subramaniam, C. Xenobiotic contamination of water by plastics and pesticides revealed through real-time, ultrasensitive, and reliable surface-enhanced raman scattering. *ACS Sustain. Chem. Eng.* **8**, 7639–7648 (2020).
26. Farrell, C. et al. Turbidity composition and the relationship with microbial attachment and UV inactivation efficacy. *Sci. Total Environ.* **624**, 638–647 (2018).
27. Saha, U., Sonon, L., Turner, P., Hawkins, G. & Mickler, K., UGA Cooperative Extension Bulletin 1487. Household water treatment: disinfection methods and devices. The University of Georgia in cooperation with Fort Valley State University, the U.S. Department of Agriculture,and counties of the state. https://secure.caes.uga.edu/extension/publications/files/pdf/B%201487_2.PDF (2018).
28. Tankersley, K. B., Dunning, N. P., Carr, C., Lentz, D. L. & Scarborough, V. L. Zeolite water purification at Tikal, an ancient Maya city in Guatemala. *Sci. Rep.* **10**, 18021 (2020).
29. Rahman, R. O. A., El-Kamash, A. M. & Hung, Y. T. Applications of nano-zeolite in wastewater treatment: an overview. *Water* **14**, 137 (2022).
30. Kyzas, G. Z. & Mitropoulos, A. C. Polymeric materials for water and wastewater management. *Polymers* **13**, 168 (2021).
31. Pradeep, T. & Anshup. Noble metal nanoparticles for water purification: a critical review. *Thin Solid Films* **517**, 6441–6478 (2009).
32. Zhou, J., Yang, F., Huang, Y., Ding, W. & Xie, X. Smartphone-powered efficient water disinfection at the point of use. *npj Clean. Water* **3**, 4886 (2020).
33. Dimapilis, E. A. S., Hsu, C. S., Mendoza, R. M. O. & Lu, M. C. Zinc oxide nanoparticles for water disinfection. *Sustain. Environ. Res.* **28**, 47–56 (2018).
34. Aragaw, T. A., Bogale, F. M. & Aragaw, B. A. Iron-based nanoparticles in wastewater treatment: a review on synthesis methods, applications, and removal mechanisms. *J. Saudi Chem. Soc.* **25**, 101280 (2021).
35. WHO and UNICEF. Silver as a drinking-water disinfectant. Alternative drinking-water disinfectants: bromine, iodine and silver. https://www.who.int/publications/i/item/9789241513692 (2018).
36. Zhang, H. Application of silver nanoparticles in drinking water purification. Open Access Diss., (2013). Paper 29. https://digitalcommons.uri.edu/oa_diss/29/.
37. Deshmukh, S. P., Patil, S. M., Mullani, S. B. & Delekar, S. D. Silver nanoparticles as an effective disinfectant: a review. *Mater. Sci. Eng. C.* **97**, 954–965 (2019).
38. Agnihotri, S., Bajaj, G., Mukherji, S. & Mukherji, S. Arginine-assisted immobilization of silver nanoparticles on ZnO nanorods: an enhanced and reusable antibacterial substrate without human cell cytotoxicity. *Nanoscale* **7**, 7415–7429 (2015).
39. Agnihotri, S., Mukherji, S. & Mukherji, S. Immobilized silver nanoparticles enhance contact killing and show highest efficacy: elucidation of the mechanism of bactericidal action of silver. *Nanoscale* **5**, 7328–7340 (2013).
40. Agnihotri, S., Mukherji, S. & Mukherji, S. Size-controlled silver nanoparticles synthesized over the range 5–100 nm using the same protocol and their antibacterial efficacy. *RSC Adv.* **4**, 3974–3983 (2014).
41. Ateia, M., Alalm, M. G., Awfa, D., Johnson, M. S. & Yoshimura, C. Modeling the degradation and disinfection of water pollutants by photocatalysts and composites: a critical review. *Sci. Total Environ.* **698**, 134197 (2020).
42. Wang, M., Ateia, M., Awfa, D. & Yoshimura, C. Regrowth of bacteria after light-based disinfection. What we know and where we go from here. *Chemosphere* **268**, 128850 (2021).
43. Nguyen, T., Roddick, F. A. & Fan, L. Biofouling of water treatment membranes: a review of the underlying causes, monitoring techniques and control measures. *Membranes* **2**, 804–840 (2012).
44. Boubault, A., Ho, C. K., Hall, A., Lambert, T. N. & Ambrosini, A. Durability of solar absorber coatings and their cost-effectiveness. *Sol. Energy Mater. Sol. C.* **166**, 176–184 (2017).
45. Kumar, S. N., Malhotra, L. K. & Chopra, K. L. Low cost electroless nickel black coatings for photothermal conversion. *Sol. Energy Mater.* **3**, 519–532 (1980).
46. Pillai, P. K. C. & Agarwal, R. C. Spectrally selective surfaces for photothermal conversion of solar energy. *Phys. Stat. Sol.* **60**, 11–25 (1980).
47. Tabor, H. Z. Receiver for solar energy collectors, US Patent 2917817, (1959).
48. Willson, K. S. Process of black chromium plating, US Patent 5861366 (1971).
49. CHROMONYX, Kewanee Oil Company, d.b.a. The Harshaw Chemical Company, SN 303,532. Pub. 4-22-69, Filed 7-24-68. Official Gazette of the United States Patent Office, Volume 864, https://books.google.co.in/books?id=b3XXzhp-R0sC&pg=PA651-IA81&lpg=PA651-IA81&dq=%22CHROMONYX,%22+Kewanee+Oil+Company&source=bl&ots=KZoomQgEWo&sig=ACfU3U25bG26h8jKAp-07HhfQDHuPerbJg&hl=en&sa=X&ved=2ahUKEwiXu6TU8o6CAxW4bWwGHXqdC_MQ6AF6BAgKEAM (1969).
50. Hottel, H. C. & Unger, T. A. Properties of a copper oxide-aluminium selective black surface absorber of solar energy. *Sol. Energy* **3**, 10–15 (1959).
51. Christie, E. A. Spectrally selective blacks for solar energy collectors. In *Proceedings of International Solar Energy Society Conference*, Melbourne, Australia, March 2–6, Paper 7/81 (1970).
52. Mar, H. Y. B., Lin, J. H., Zimmer, P. B., Peterson, R. E. & Gross, J. S. *Optical coatings for flat plate solar collectors*. Final report, 16, United States, U.S. Department of Energy, Office of Scientific and Technical Information. https://www.osti.gov/biblio/7339553 (U.S. Department of Energy, Office of Scientific and Technical Information, 1975).

53. Henry, A., Prasher, R. & Majumdar, A. Five thermal energy grand challenges for decarbonization. *Nat. Energy* **5**, 635–637 (2020).
54. Zhang, K. et al. A review on thermal stability and high temperature induced ageing mechanisms of solar absorber coatings. *Renew. Sust. Energy Rev.* **67**, 1282–1299 (2017).
55. Noč, L. et al. High-solar-absorptance CSP coating characterization and reliability testing with isothermal and cyclic loads for service-life prediction. *Energy Environ. Sci.* **12**, 1679–1694 (2019).
56. Ho, C. K. et al. Characterization of Pyromark 2500 paint for high-temperature solar receivers. *Sol. Energy Eng.* **136**, 014502 (2014).
57. Torres, J. F. et al. Highly efficient and durable solar thermal energy harvesting via scalable hierarchical coatings inspired by stony corals. *Energy Environ. Sci.* **15**, 1893–1906 (2022).
58. Xu, K. et al. A review of high-temperature selective absorbing coatings for solar thermal applications. *J. Materiomics* **6**, 167–182 (2020).
59. Maity, A. & Polshettiwar, V. Dendritic fibrous nanosilica for catalysis, energy harvesting, carbon dioxide mitigation, drug delivery, and sensing. *ChemSusChem* **10**, 3866–3913 (2017).
60. Saha, J., Ball, R., Sah, A., Kalyani, V. & Subramaniam, C. The mechanistic role of a support catalyst interface in electrocatalytic water reduction by Co_3O_4 supported nanocarbon florets. *Nanoscale* **11**, 13532–13540 (2019).
61. Moronshing, M., Sah, A., Kalyani, V. & Subramaniam, C. Nanostructured carbon florets as scavenger of As^{3+}, Cr^{6+}, Cd^{2+} and Hg^{2+} for water remediation. *ACS Appl. Nano Mater.* **3**, 468–478 (2020).
62. Jha, M. K. et al. Hierarchically engineered nanocarbon florets as bifunctional electrode material for adsorptive and intercalative energy storage. *ACS Appl. Mater. Interfaces* **12**, 42669–42677 (2020).
63. Sharma, S., Sah, A., Subramaniam, C. & Saha, S. K. Performance enhancement of tapered helical coil receiver using novel nanostructured carbon florets coating. *Appl. Therm. Eng.* **194**, 117065 (2021).
64. Dwivedi, I. & Subramaniam, C. Joule heating-driven transformation of hard-carbons to onion-like carbon monoliths for efficient capture of volatile organic compounds. *ACS Mater. Au* **2**, 154–162 (2022).
65. Sah, A., Sharma, S., Saha, S. & Subramaniam, C. Phonon-engineered hard-carbon nanoflorets achieving rapid and efficient solar-thermal based water evaporation and space-heating. *ACS Appl. Mater. Interfaces* **15**, 43810–43821 (2023).
66. Weaving, J. S. et al. Elucidating the sodiation mechanism in hard carbon by operando raman spectroscopy. *ACS Appl. Energy Mater.* **3**, 7474–7484 (2020).
67. Saito, R., Hofmann, M., Dresselhaus, G., Jorio, A. & Dresselhaus, M. S. Raman spectroscopy of graphene and carbon nanotubes. *Adv. Phys.* **60**, 413–550 (2011).
68. Subramaniam, C. et al. Visible fluorescence induced by the metal semiconductor transition in composites of carbon nanotubes with noble metal nanoparticles. *Phys. Rev. Lett.* **99**, 167404 (2007).
69. Young H. D., Freedman R. A. & Ford A. L. *University physics*, 12th ed. (Pearson, 2009).
70. George, J., Nagaraja, S. K. & Ajisha, A. Assessment of microbiological and physico-chemical characterıstics of water samples in households of Bangalore city, Karnataka, India. *J. Water Sanit. Hyg. Dev.* **11**, 416–422 (2021).
71. Begum, M. et al. Indian coastal waters: a concoction of sewage indicator bacteria! An assessment on recreational beaches. *Environ. Monit. Assess.* **193**, 455 (2021).
72. Harwood, V. et al. General and host-associated bacterial indicators of faecal pollution. Global Water Pathogen Project. https://doi.org/10.14321/waterpathogens.6 (2018).
73. Atkins, P. & Julio de P. *Physical chemistry for the life sciences* (W.H. Freeman and Company, 2006), 282–288.
74. Moronshing, M. & Subramaniam, C. Scalable approach to highly efficient and rapid capacitive deionization with cnt-thread as electrodes. *ACS Appl. Mater. Interfaces* **9**, 39907–39915 (2017).
75. Ahammed, M. M. & Davra, K. Performance evaluation of biosand filter modified with iron oxide-coated sand for household treatment of drinking water. *Desalination* **276**, 287–293 (2011).

ACKNOWLEDGEMENTS

AS acknowledges Aslam Villan for helping with the photograph and video of SWAP. A.S. acknowledges Sophisticated Analytical Instrument Facility (SAIF), IIT-Bombay, Central Facility for the required instrumentation.

AUTHOR CONTRIBUTIONS

A.S.- conceptualization, methodology, experimentation, investigation, data visualization and interpretation, writing-original draft, review & editing. A.K.M.- Providing initial bacterial cell, Training for bacterial experiment. S.T.- Designing of coil 3D schematic, flow controller and automated setup for SWAP, writing code for SWAP. S.M.- conceptualization, data visualization and interpretation, writing- review and editing, supervision. C.S.- conceptualization, methodology, data visualization and interpretation, writing- original draft, review & editing, supervision, funding acquisition.

FUNDING

C.S. thanks the Department of Science and Technology, Government of India for generous support through grants DST/TMD/MES/2k17/41 and SERB/F/9022/2019-2020. AS thanks the Council of Scientific and Industrial Research, India for their support.

COMPETING INTERESTS

The authors declare no competing interests.

ADDITIONAL INFORMATION

Supplementary information The online version contains supplementary material available at https://doi.org/10.1038/s41545-023-00284-4.

Correspondence and requests for materials should be addressed to Soumyo Mukherji or Chandramouli Subramaniam.

Reprints and permission information is available at http://www.nature.com/reprints

Publisher's note Springer Nature remains neutral with regard to jurisdictional claims in published maps and institutional affiliations.